



# Electric Propulsion Architecture Assessment via Signomial Programming

Aidan P. Dowdle\*, David K. Hall†, and Jeffrey H. Lang‡  
*Massachusetts Institute of Technology, Cambridge, MA, 02139, U.S.A.*

**This paper presents the application of signomial programming to the assessment and multi-disciplinary optimization of electric propulsion systems. Analytic models for electrical and mechanical propulsion system components are developed that are compatible with the signomial programming objective and constraint forms. These models capture the dependence of mass and efficiency on material properties and operating conditions. Standalone optimization of the electrical cable and motor model illustrates a trade-off between mass and efficiency at the component level. These component models are subsequently integrated into various propulsion architectures and are optimized while taking into account the component dependencies (e.g., fan and motor shaft speed). Specifically, turbofan, turboelectric and geared turboelectric propulsion architectures are optimized on the metrics of fuel consumption and propulsion system mass. The results show that the optimal component masses and efficiencies depend on the propulsion architecture, operating point, and performance metric under consideration, and that signomial programming is useful for determining them.**

## Nomenclature

$A$	=	area
$B$	=	magnetic flux density
$BSE$	=	battery specific energy
$BSP$	=	battery specific power
$d$	=	material density, diameter
$E$	=	electric field
$f$	=	frequency [Hz]
$g$	=	machine air gap thickness
$h_{\text{fuel}}$	=	fuel heating value
$I$	=	current
$J$	=	current density
$K$	=	component mass scaling constant
$k_e$	=	eddy loss coefficient
$k_h$	=	hysteresis loss coefficient
$k_{\text{pf}}$	=	packing factor
$L_{\text{et}}$	=	end turn length
$\ell$	=	length
$m$	=	mass
$\dot{m}$	=	mass flow
$M$	=	magnetization constant
$P$	=	power
$P_{\text{sp}}$	=	core specific power
$PMR$	=	electric component power-to-mass ratio
$p$	=	number of pole pairs
$R$	=	resistance, radius
$T, t$	=	thickness

\*Graduate Research Assistant, Dept. of Electrical Engineering and Computer Science, email: adowdle@mit.edu, Member AIAA.

†Research Engineer, Dept. of Aeronautics and Astronautics, Member AIAA.

‡Professor of Electrical Engineering, Dept. of Electrical Engineering and Computer Science

$U$	=	tip speed
$V$	=	voltage
$V_{\text{jet}}$	=	propulsor jet velocity
$V_{\infty}$	=	free stream velocity
$W$	=	width
$\alpha$	=	exponential fit coefficient
$\beta$	=	gearbox scaling parameter
$\eta$	=	efficiency
$\eta_{\text{th}}$	=	cycle thermal efficiency
$\lambda$	=	slot fill fraction
$\mu_0$	=	vacuum permeability constant
$\rho_{\infty}$	=	resistivity
$\tau$	=	torque
$\phi$	=	magnetic flux
$\Omega$	=	shaft angular speed
$\omega$	=	frequency [rad/s]

### Subscripts

bat	=	battery
cond	=	conductor
core	=	gas generator core
$e, \text{elec}$	=	electric
int	=	internal
gb	=	gearbox
$m$	=	magnets
mech	=	mechanical
ph	=	per-phase
$r$	=	rotor
rms	=	root mean square
$s$	=	stator
rbi	=	rotor back iron
sat	=	saturation
sbi	=	stator back iron
$t$	=	teeth
tot	=	total
wind	=	windings

## I. Introduction

Advancements in battery, power electronic, and electrical generator/motor technology have led to renewed interest in researching the potential of electric propulsion to improve aircraft performance. Specifically, electric propulsion is viewed as having the potential to enable short take-off and landing, reduce fuel burn, produce less noise, and cut back on emissions for aircraft [1]. Despite the additional weight and inefficiencies added from using electrical distribution, several single-point, conceptual designs have shown that electric propulsion can provide an overall system-level benefit with respect to these metrics [1, 2]. However, some designs use a battery as the only energy source, whereas others use hybrid (battery and fuel-based) propulsion or just conventional turbofans. In fact, there are many propulsion architectures possible, as identified in Ref. [3] and shown in Fig. 1.

The propulsion systems in Fig. 1 contain a mix of chemical, electrical and mechanical components whose size and performance vary with power and energy requirements and the design of the device. To estimate the mass and performance of these systems, one approach is to use a constant specific power, or power-to-mass ratio, and efficiency for each component. A specific power assumes that the mass of a component scales linearly with its input power, whereas a constant efficiency assumes the same fraction of the input power is lost in transmission regardless of input power

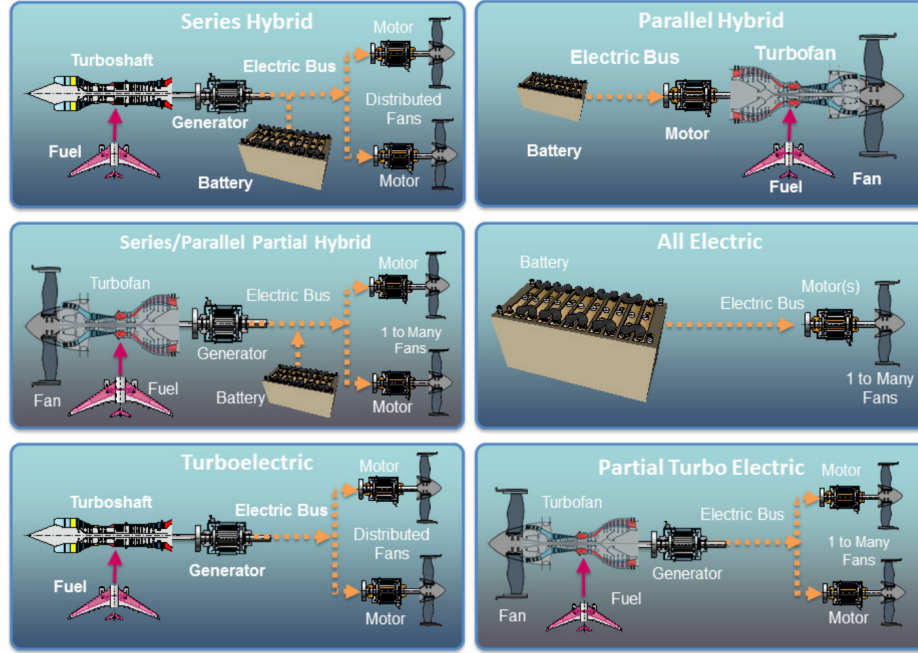


**Fig. 1 Survey of possible electric propulsion architectures [3].**

magnitude. State-of-the-art values for these parameters can be obtained from Ref. [4].

Constant specific powers and efficiencies have been used in the turboelectric concept assessments in Refs. [5] and [6], and a recent trade space study in Refs. [7] and [8]. However, a survey on motor power-to-mass ratios, shown in Fig. 2, shows that specific power is not constant across rated power [9]. Generally, motor specific power improves at lower power levels, but even then spans a wide range. This spread could be explained, for example, from some of the reported specific powers including the thermal management system mass, from the materials used, or from the torque/speed requirement. Moreover, the efficiencies of electrical components depend on their operating point. For example, a high voltage distribution system has lower losses than a low voltage system for the same power delivered because the losses are proportional to current squared. These nonlinear trends in specific power and efficiency motivate the use of higher fidelity models in system level studies prior to more detailed design.

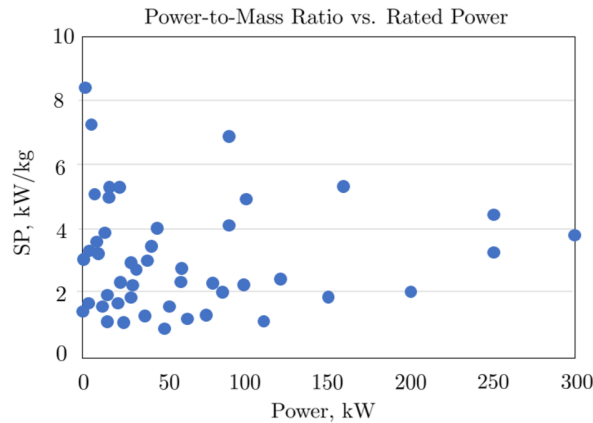


**Fig. 2 Survey of motor power-to-mass ratios versus rated power [9].**

This paper uses an optimization technique called signomial programming to assess electric propulsion systems that use component models which capture the aforementioned nonlinear trends. Section II summarizes the signomial programming optimization technique and the types of models used for propulsion components. Next, Section III

develops the analytic expressions used in the more detailed electric component models. Similarly, Section IV explains the theory for the mechanical components. The ability of these more detailed models to capture specific power and efficiency trends is demonstrated in Section V. Section VI shows how these models can be interconnected for optimization of the different propulsion architectures. Finally, Section VII discusses the results and identifies areas for future work.

## II. Modeling Approach

### A. Signomial Programming

The sizing and performance of the propulsion system is cast as a non-linear optimization problem called a *signomial program* (SP) [10]. This type of problem is a more general version of a *geometric program* (GP), which is an optimization problem that has a nonlinear objective and constraint form, but is convex via a log-space transform. Due to this property, a GP can be solved rapidly, guarantees a globally optimal solution, and provides sensitivities to the problem inputs [11].

An SP cannot be converted into convex form and thus loses the global optimum guarantee of a GP, but allows for a more general form of objectives and constraints. In addition, SPs are solved as a sequence of local GP approximations, so SPs can likewise be rapidly solved and provide sensitivities to problem inputs [11]. An SP has the form

$$\begin{aligned} & \underset{x}{\text{minimize}} && f_0(x) \\ & \text{subject to} && f_i(x) \leq 1, \quad i = 1, \dots, m \\ & && f_j(x) = 1, \quad j = m + 1, \dots, n \end{aligned}$$

where  $x$  is a vector of strictly positive decision variables, and the objective and constraints are signomial functions

$$f(x) = \sum_{k=1}^K c_k x_1^{a_{1,k}} x_2^{a_{2,k}} \dots x_n^{a_{n,k}} \quad (1)$$

where  $c_k, a_{i,k} \in \mathbb{R}$ .

An example of a commonly used signomial equality constraint is Kirchoff's voltage law. For the battery model described in Section III, this results in

$$V_{\text{bat}} = IR_{\text{int}} + V_{\text{load}} \quad (2)$$

where  $V_{\text{bat}}$  is the battery voltage,  $V_{\text{load}}$  is the load voltage,  $I$  is the current, and  $R_{\text{int}}$  is the internal battery resistance. This is alternatively written as

$$\frac{IR_{\text{int}}}{V_{\text{bat}}} + \frac{V_{\text{load}}}{V_{\text{bat}}} = 1 \quad (3)$$

which is a signomial function with

$$\begin{aligned} (x_1, x_2, x_3, x_4) &= (I, R_{\text{int}}, V_{\text{load}}, V_{\text{bat}}) \\ (c_1, c_2) &= (1, 1) \\ (a_{1,1}, a_{2,1}, a_{3,1}, a_{4,1}) &= (1, 1, 0, -1) \\ (a_{1,2}, a_{2,2}, a_{3,2}, a_{4,2}) &= (0, 0, 1, -1). \end{aligned} \quad (4)$$

A Python package called GPKit [10] was used to define and solve the electric propulsion SPs in this paper.

### B. Propulsion Components Modeled

The propulsion system components are developed as individual model classes in the GPKit framework [10] and connected using power, torque, speed, frequency, voltage and current constraints where applicable. This modular approach allows component models to be developed at different levels of fidelity which are summarized in Table 1. The components are divided into sizing and performance models, with the former containing decision variables and constraints that cannot change over the course of the mission (e.g., fan diameter), and the latter containing those that can (e.g., fan speed). The next two sections explain the theory for these components.

**Table 1 Propulsion component models.**

Sub-system	Components	Sizing Model	Performance Model
Electric	Battery	specified energy and power densities	voltage-resistor circuit
	Power Electronics	specified power density	specified efficiency
	Cable	voltage-current sizing	resistor circuit
	Generator/Motor	torque-speed sizing	single-phase equivalent circuit
Mechanical	Gas generator core	mass flow power-law scaling	specified thermal efficiency
	Ducted fan	mass flow power-law scaling	specified efficiency
	Gearbox	empirical data fit	specified efficiency

### III. Electrical Component Models

#### A. Battery Pack

##### 1. Battery Pack Sizing

The battery mass  $m_{\text{bat}}$  is sized using pack-level energy-to-mass (*BSE*) and power-to-mass (*BSP*) ratios. That is,

$$\begin{aligned} m_{\text{bat}} &= E_{\text{bat,tot}}/BSE \\ m_{\text{bat}} &= P_{\text{bat,max}}/BSP \end{aligned} \quad (5)$$

where  $E_{\text{bat,tot}}$  is the total energy the battery must supply for the mission, and  $P_{\text{bat,max}}$  is the maximum power the battery needs to provide.

##### 2. Battery Pack Performance

The efficiency of the battery is a function of the load (e.g., motor) it is supplying. Since the battery is sized based on load power and energy rather than voltage and current, this section will show how the efficiency can likewise be expressed in terms of the power it is sized for and the load power. Specifically, the battery efficiency,  $\eta_{\text{bat}}$ , is related via

$$4\eta_{\text{bat}}(1 - \eta_{\text{bat}}) = P_{\text{load}}/P_{\text{bat,max}} \quad (6)$$

where  $P_{\text{load}}$  is the load power and  $P_{\text{bat,max}}$  is the maximum battery power.

Equation 6 is derived from the equivalent voltage-resistor model for the battery, shown in Fig. 3. In this diagram,  $V_{\text{bat}}$  is the battery pack design voltage,  $R_{\text{int}}$  is the internal battery resistance, and  $V_{\text{load}}$  is the voltage across the battery terminals. From Kirchoff's voltage law, the load voltage,  $V_{\text{load}}$ , is a function of the battery voltage via

$$V_{\text{load}} = V_{\text{bat}} - IR_{\text{int}}. \quad (7)$$

The delivered power to the load is then

$$\begin{aligned} P_{\text{load}} &= IV_{\text{load}} \\ &= IV_{\text{bat}} - I^2R_{\text{int}}. \end{aligned} \quad (8)$$

The maximum of this power occurs when the derivative of Eqn. (8) with respect to current is zero, or  $I = V_{\text{bat}}/(2R_{\text{int}})$ . The corresponding maximum deliverable load power is

$$P_{\text{load,max}} = \frac{V_{\text{bat}}^2}{4R_{\text{int}}} \quad (9)$$

which shows that the maximum deliverable power is fixed by the battery pack design.

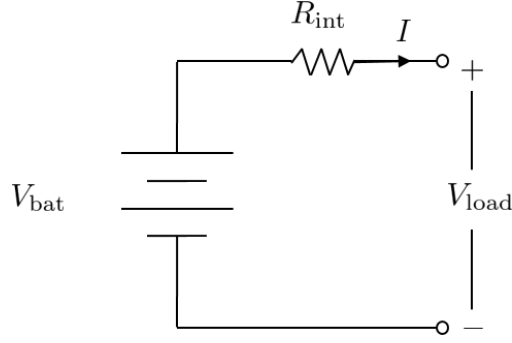


**Fig. 3** The battery is modeled as a constant voltage source and series resistor.

The efficiency of the battery for a given load is expressed in terms of power by dividing Eqn. (8) and Eqn. (9):

$$\begin{aligned}
 \frac{P_{\text{load}}}{P_{\text{load,max}}} &= \frac{IV_{\text{bat}} - I^2 R_{\text{int}}}{\frac{V_{\text{bat}}^2}{4R_{\text{int}}}} \\
 &= 4 \left( 1 - \frac{IR_{\text{int}}}{V_{\text{bat}}} \right) \left( \frac{IR_{\text{int}}}{V_{\text{bat}}} \right) \\
 &= 4 \left( 1 - \frac{I^2 R_{\text{int}}}{IV_{\text{bat}}} \right) \left( \frac{I^2 R_{\text{int}}}{IV_{\text{bat}}} \right) \\
 &= 4\eta_{\text{bat}} (1 - \eta_{\text{bat}})
 \end{aligned} \tag{10}$$

where the last equality is derived from recognizing that  $I^2 R_{\text{int}}$  is the ohmic heating losses and  $IV_{\text{bat}}$  is the source power, therefore  $1 - I^2 R_{\text{int}}/(IV_{\text{bat}})$  is the battery efficiency,  $\eta_{\text{bat}}$ , whereas the term  $I^2 R_{\text{int}}/(IV_{\text{bat}})$  is its inefficiency,  $1 - \eta_{\text{bat}}$ . Thus, the use of Eqn. (6) is equivalent to using a series voltage-resistor battery model.

## B. Power Electronics

### 1. Power Electronics Sizing

The size of the power electronics is assumed to scale linearly with rated power by a specific value power  $PMR_{\text{p.e.}}$ . Since the power can vary over the course of an aircraft mission, the power electronics mass,  $m_{\text{p.e.}}$ , is sized based on its maximum input power,  $P_{\text{in,max}}$ :

$$m_{\text{p.e.}} = P_{\text{in,max}} / PMR_{\text{p.e.}} \tag{11}$$

### 2. Power Electronics Performance

The power electronics is assumed to have a fixed efficiency over its entire power operating range. That is,

$$P_{\text{out}} = \eta_{\text{p.e.}} P_{\text{in}} \tag{12}$$

## C. Cable

### 1. Cable Sizing

The cable model assumes a cylindrical geometry with an inner conductor layer and outer insulation layer. The insulation is sized to prevent dielectric breakdown and the conductor is sized based on tolerable Ohmic heating losses. Figure 4 shows that the cable geometry consists of an inner radius  $a$  and outer radius  $b$ . The conductor is assumed to use stranded (i.e., Litz) wire that mitigates the skin and proximity effects - loss mechanisms due to AC signals. Since there is space between the strands, the fraction of the  $a$ -radius cylinder that the conductive material actually occupies is the packing factor,  $k_{\text{pf}}$ .

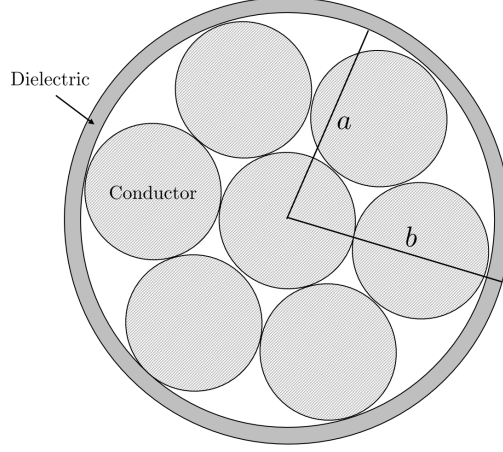


**Fig. 4 Cable cross-section geometry showing the conductor and dielectric regions.**

The conductor cross-sectional area,  $A_c$ , is

$$A_c = \pi a^2 k_{pf} \quad (13)$$

and the dielectric cross-sectional area,  $A_{di}$ , is

$$\begin{aligned} A_{di} &= \pi (b^2 - a^2) \\ &= \pi (b + a) t_{di} \end{aligned} \quad (14)$$

where  $t_{di} = b - a$  is this thickness of the dielectric. The mass of the cable, assuming a length  $\ell_c$ , conductor density  $d_c$ , and dielectric density  $d_{di}$ , is

$$m_c = A_c \ell_c d_c + A_{di} \ell_c d_{di} \quad (15)$$

Dielectric breakdown occurs when the electric field in the cable insulation exceeds  $E_{\max}$ , a dielectric material property. Assuming the dielectric thickness is small, a parallel-plate approximation for the electric field is sufficient. The maximum electric field strength is

$$E_{\max} = \frac{V_{\max}}{t_{di}} \quad (16)$$

where  $V_{\max}$  is the maximum voltage across the cable.

The resistance of the cable is given by

$$R_c = \rho \frac{\ell_c}{A_c} \quad (17)$$

where  $\rho$  is the resistivity of the cable.

## 2. Cable Performance

To capture the efficiency of the cable as a function of its input/output voltages in both standalone and system-level optimization, the cable is modeled as a resistor, shown in Fig. 5. From Kirchhoff's voltage law,

$$V_{\text{load}} + IR_c = V_{\text{source}} \quad (18)$$

The Ohmic heating losses are

$$Q_{\text{ohmic},c} = I^2 R_c \quad (19)$$

and the load and source powers are

$$P_{\text{load}} = IV_{\text{load}} \quad (20)$$

$$P_{\text{source}} = IV_{\text{source}} \quad (21)$$

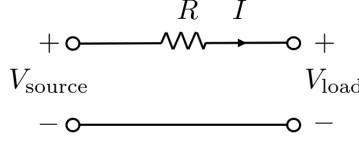


**Fig. 5** The cable appears as a resistor when connected to other components.

#### D. Generators and Motors

The electrical generator and motor models share the same basic geometry and are considered together in this section as electrical machines. There are a variety of electrical machine types to choose from, such as permanent magnet, induction, and variable reluctance, that each have their own advantages and disadvantages. In this paper, a tooth-and-slot, permanent magnet synchronous machine is modeled. This geometry was chosen because it is a common electrical machine type that has been successful in yielding high efficiency, high torque density machines, such as those in Ref. [12] and Ref. [13].

##### 1. Electrical Machine Sizing

The permanent magnet electrical machine model is considered to consist of five different components: a stator back iron, stator teeth, windings, magnets, and a rotor back iron. The layout of these components in an electrical machine is shown in Fig. 6.

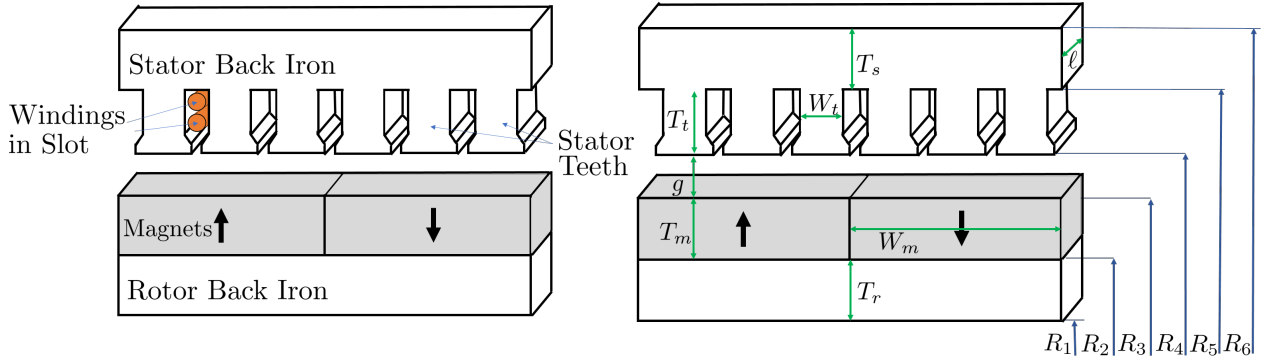


**Fig. 6** Electrical machine cross-sections showing the components (left) and dimensions (right).

It is assumed that this is a three phase machine with three slots per pole. In addition, the machine presented here has the rotor interior to the stator, but the model can be modified to represent an outer rotor geometry.

**Rotor Back Iron** The rotor back iron supports the magnets and confines the magnetic flux they generate. The mass of the rotor back iron is the product of the area of the annulus it occupies,  $A_{rbi}$ , the axial length of the machine,  $\ell$ , and the density of the rotor,  $d_{rotor}$ . Since the rotor has an inner radius,  $R_1$ , and outer radius,  $R_2$ , the mass  $m_{rbi}$  is thus

$$\begin{aligned} m_{rbi} &= A_{rbi} \ell d_{rotor} \\ &= \pi (R_2^2 - R_1^2) \ell d_{rotor} \\ &= \pi (R_2 + R_1) T_r \ell d_{rotor} \end{aligned} \quad (22)$$

where the rotor thickness,  $T_r = R_2 - R_1$ , is substituted to obtain the last expression.

The rotor thickness variable is used because it is sized to carry the magnet flux. Assuming the average magnetic flux density in the air gap is  $B_{gap}$ , the total air gap flux,  $\phi_{gap}$ , passing through the air gap interface,  $A_{gap}$ , is approximately

$$\begin{aligned} \phi_{gap} &= B_{gap} A_{gap} \\ &= B_{gap} 2\pi R_3 \ell. \end{aligned} \quad (23)$$



Similarly, the rotor back iron flux  $\phi_{rbi}$  is related to the rotor back iron flux density,  $B_{rbi}$ , and cross section area,  $A_{rbi}$ , via

$$\begin{aligned}\phi_{rbi} &= B_{rbi} A_{rbi} \\ &= B_{rbi} T_r \ell.\end{aligned}\quad (24)$$

Next, from the three slots per pole assumption, assuming  $p$  pole pairs, there are  $6p$  teeth in the electrical machine. Assuming all the flux passes through the teeth/back iron (i.e., that there is no leakage flux), the magnetic flux through a single tooth is

$$\begin{aligned}\phi_{tooth} &= B_{gap} \frac{A_{gap}}{6p} \\ &= \frac{\phi_{gap}}{6p}.\end{aligned}\quad (25)$$

The peak flux through the back iron is  $3/2$  times the tooth flux. This  $3/2$  factor comes from the flux in one tooth being “split” between two poles. The flux paths are shown in Fig. 7.

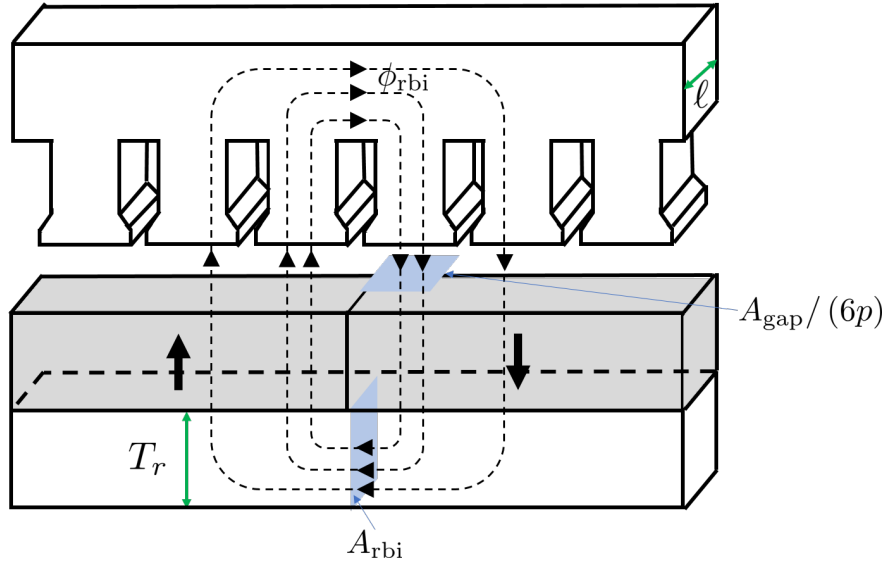


**Fig. 7** Diagram showing the flux path when the rotor back iron is exposed to peak flux.

From equating the rotor back iron and tooth fluxes, the rotor back iron flux is

$$\phi_{rbi} = \frac{3}{2} \frac{\phi_{gap}}{6p}.\quad (26)$$

Substituting Eqn. (24) and Eqn. (23) into Eqn. (26) and rearranging, the necessary rotor thickness is

$$T_r = \frac{B_{gap}}{B_{rbi}} \frac{\pi R_3}{2p}\quad (27)$$

where the rotor back iron flux density,  $B_{rbi}$  must be less than the steel saturation flux density,  $B_{sat}$ .

**Magnets** The magnets have inner radius  $R_2$  and outer radius  $R_3$ . Assuming a magnet density  $d_{mag}$ , the mass of the magnets,  $m_{mag}$ , is

$$\begin{aligned}m_{mag} &= \pi (R_3^2 - R_2^2) \ell d_{mag} \\ &= \pi (R_3 + R_2) T_m \ell d_{mag}.\end{aligned}\quad (28)$$

where  $T_m = R_3 - R_2$  is the magnet thickness.

The magnet thickness is related to the air gap flux density,  $B_{\text{gap}}$ , which depends on the torque requirement of the machine. The relation between the magnet thickness and  $B_{\text{gap}}$  is

$$B_{\text{gap}} = \frac{\mu_0 M T_m}{T_m + g} \quad (29)$$

where  $\mu_0$  is the vacuum permeability constant,  $M$  is the magnetization constant, and  $g$  is the air gap thickness. Equation (29) is derived from considering the magnetic circuit of the flux path in Fig. 7, excluding the mmf drop across the electrical machine steel.

**Stator Teeth** The stator teeth effectively shorten the air gap,  $g$ , of the machine and thus improve the air gap flux density via Eqn. (29). The stator teeth are assumed to be rectangular with thickness  $T_t$  and width  $W_t$ . From the three slots per pole assumption, there are six teeth per pole pair or  $6p$  teeth total. The total teeth area,  $A_{\text{teeth}}$  is

$$A_{\text{teeth}} = 6p T_t W_t \quad (30)$$

and the total teeth mass is

$$m_{\text{teeth}} = A_{\text{teeth}} \ell d_{\text{stator}} \quad (31)$$

Similar to the rotor back-iron, the teeth are sized based on the air gap magnetic flux density generated from the permanent magnets. However, another effect considered that can significantly limit electrical machine performance is the magnetic field generated from the windings in the slots, also referred to as the armature reaction [14]. Assuming the motor has a maximum usable current density  $J_m$ , the magnetic flux density,  $B_{\text{wind}}$ , generated from the winding current is

$$B_{\text{wind}} = \mu_0 J_m T_t \quad (32)$$

This armature reaction adds vectorially to the teeth flux passed from the permanent magnets. The latter is the airgap flux density divided by  $\lambda$ , the ratio of the slot width to the slot pitch. The magnitude of the teeth flux density is thus the magnitude of the vector sum of the air gap flux density contribution and armature reaction [14]:

$$\left( \frac{B_{\text{gap}}}{\lambda} \right)^2 + B_{\text{wind}}^2 = B_{\text{teeth}}^2 \leq B_{\text{sat}}^2 \quad (33)$$

**Windings** The windings are wrapped around the teeth to link the magnetic flux from the magnets and generate a torque on the rotor. These windings are placed in slots next to the teeth. Since the teeth were assumed to be rectangular, the total slot area,  $A_{\text{slots}}$ , is solved for by subtracting the total teeth area from the ring that both the teeth and the slots occupy. The inner radius of this ring is  $R_4$  and the outer radius is  $R_5$ , so the areas sum to

$$\begin{aligned} A_{\text{teeth}} + A_{\text{slots}} &= \pi (R_5^2 - R_4^2) \\ &= \pi (R_5 + R_4) T_t \end{aligned} \quad (34)$$

Similar to the Litz wire in the cable model, the windings only occupy a fraction  $k_{\text{pf}}$  of the available slot area. The mass of the windings inside the slots,  $m_{\text{wind,main}}$ , assuming a conductor density  $d_{\text{cond}}$ , is

$$m_{\text{wind,main}} = k_{\text{pf}} A_{\text{slots}} \ell d_{\text{cond}} \quad (35)$$

The part of the winding that wraps around the outside of the machine is referred to as the end winding and contributes to resistive losses, but not torque production. The length of these end windings is modeled assuming a triangular pattern, the derivation of which can be found in Ref. [13]. The length of the hypotenuse of these triangular end turns,  $L_{\text{et}}$ , is

$$L_{\text{et}} = \frac{\pi}{2p} R_4 \frac{\lambda}{\sqrt{1 - \lambda^2}} \quad (36)$$

Having defined  $A_{\text{slots}}$ ,  $\lambda$  can now be expressed explicitly as

$$\lambda = \frac{A_{\text{slots}}}{A_{\text{slots}} + A_{\text{teeth}}} \quad (37)$$

The total winding mass,  $m_{\text{wind}}$ , is the sum of the contribution from the main windings and end windings:

$$m_{\text{wind}} = k_{\text{pf}} A_{\text{slots}} (\ell + 2L_{\text{et}}) d_{\text{cond}} \quad (38)$$

**Stator Back Iron** Let  $m_{\text{sbi}}$  be the mass of the stator back iron. The stator back iron is sized in the same manner as the rotor back iron, but at different radii. Assuming the stator back iron has an inner radius  $R_5$  and outer radius  $R_6$ , its mass is

$$\begin{aligned} m_{\text{sbi}} &= A_{\text{sbi}} \ell d_{\text{stator}} \\ &= \pi (R_6^2 - R_5^2) \ell d_{\text{stator}} \\ &= \pi (R_6 + R_5) T_s \ell d_{\text{stator}} \end{aligned} \quad (39)$$

where  $T_s$  is the stator back iron thickness, sized to carry the air gap flux from the magnets.:

$$T_s = \frac{B_{\text{gap}}}{B_{\text{sbi}}} \frac{\pi R_3}{2p} \quad (40)$$

and  $B_{\text{sbi}} \leq B_{\text{sat}}$ .

**Total Electrical Machine Mass** The total electrical machine mass is the sum of its constituents:

$$m_{\text{motor}} = m_{\text{sbi}} + m_{\text{teeth}} + m_{\text{wind}} + m_{\text{mag}} + m_{\text{rbi}}. \quad (41)$$

**Resistance** The area of a single slot is  $A_{\text{slot}} = A_{\text{slots}}/(6p)$ . The resistance of the windings in one slot is

$$R_{\text{slot}} = \rho \left( \frac{\ell + 2L_{\text{et}}}{k_{\text{pf}} A_{\text{slot}}} \right). \quad (42)$$

Since there are  $6p$  slots, the total resistance is  $6pR_{\text{slot}}$ . From the three phase assumption, the phase resistance used for estimating Ohmic heating losses can be calculated as one third of the total resistance, or

$$R_{\text{ph}} = 2p\rho \left( \frac{\ell + 2L_{\text{et}}}{k_{\text{pf}} A_{\text{slot}}} \right). \quad (43)$$

The winding area,  $k_{\text{pf}} A_{\text{slot}}$ , is limited by the available slot area, wire area, and number of turns used to link the magnetic flux. This constraint is captured via

$$\begin{aligned} A_{\text{wire}} &= k_{\text{pf}} A_{\text{slot}} / N \\ A_{\text{wire}} &\geq A_{\text{wire, min}} \end{aligned} \quad (44)$$

where  $A_{\text{wire, min}}$  is based on empirical data.

## 2. Electrical Machine Performance

**Mechanical Power** The electrical machine torque is expressed as the product of the Lorentz force on the current carrying conductors and the moment arm. For this motor model, the current per slot,  $I_{\text{slot}}$ , is

$$I_{\text{slot}} = J_s k_{\text{pf}} A_{\text{slot}} \quad (45)$$

where  $J_s$  is the peak slot current density. Assuming two phases are excited at any given time, two-thirds of the slots or  $4p$  slots are carrying this current. Since the end turns do not contribute to torque production, the total Lorentz force,  $F$ , is then

$$F = 4p B_{\text{gap}} J_s k_{\text{pf}} A_{\text{slot}} \ell \quad (46)$$

Approximating the moment arm at the air gap radius,  $R_3$ , the torque is

$$\tau = 4p R_3 B_{\text{gap}} J_s k_{\text{pf}} A_{\text{slot}} \ell \quad (47)$$

which explicitly relates torque and current.

With an expression for torque developed, the total mechanical power is then

$$P_{\text{mech}} = \tau \Omega = 4p R_3 B_{\text{gap}} J_s k_{\text{pf}} A_{\text{slot}} \ell \Omega \quad (48)$$

where angular speed,  $\Omega$ , is limited by a specified tip speed (burst) limit,  $U_{\text{max}}$ :

$$U = R_3 \Omega \leq U_{\text{max}}. \quad (49)$$

The angular speed is related to electrical frequency,  $f$ , via

$$\Omega = \frac{2\pi f}{p}. \quad (50)$$

**Electrical Power** The motor is assumed to be controlled via sinusoidal currents. A single phase current is described via

$$I(\omega_e t) = I_0 \sin(\omega_e t) \quad (51)$$

where  $I_0$  is the peak current,  $\omega_e$  is electrical frequency, and  $t$  is time. The corresponding back-emf is assumed to have the square-wave shape,

$$V(\omega_e t) = \begin{cases} V_0, & 2\pi k \leq \omega_e t < \pi(2k+1) \\ -V_0, & \pi(2k+1) \leq \omega_e t < 2\pi(k+1) \end{cases} \quad (52)$$

where  $k$  is an integer.

Therefore, the average power for one phase,  $P_{\text{elec,ph}}$ , computed over one period is

$$\begin{aligned} P_{\text{elec,ph}} &= \frac{1}{2\pi} \int_0^{2\pi} I(\omega_e t) V(\omega_e t) d(\omega_e t) \\ &= \frac{1}{2\pi} \left[ \int_0^\pi I_0 V_0 \sin(\omega_e t) d(\omega_e t) - \int_\pi^{2\pi} I_0 V_0 \sin(\omega_e t) d(\omega_e t) \right] \\ &= \frac{2V_0 I_0}{\pi} \end{aligned} \quad (53)$$

which can be expressed in terms of RMS voltages and currents as

$$P_{\text{elec,ph}} = \frac{2\sqrt{2}V_{\text{rms}}I_{\text{rms}}}{\pi}. \quad (54)$$

The total average electrical power is the sum of the three average phase powers,

$$P_{\text{elec}} = \frac{6\sqrt{2}I_{\text{rms}}V_{\text{rms}}}{\pi}. \quad (55)$$

**Losses and Power Balance** The angular speed and voltage are related via a power balance, accounting for Ohmic heating, eddy current, and hysteresis losses. For a motor,

$$P_{\text{elec}} = P_{\text{mech}} - Q_{\text{ohmic}} - Q_{\text{eddy}} - Q_{\text{hysteresis}} \quad (56)$$

whereas for a generator the electrical and mechanical power terms are swapped. The Ohmic heating losses are

$$Q_{\text{ohmic}} = I^2 (2R_{\text{ph}}) \quad (57)$$

The electrical machine model is completed by characterizing the eddy current and hysteresis losses [13]:

$$\begin{aligned} Q_{\text{eddy}} &= m_{\text{sbi}} \left( k_e f^2 B_{\text{sbi}}^2 \right) + m_{\text{teeth}} \left( k_e f^2 B_{\text{teeth}}^2 \right) \\ Q_{\text{hyst}} &= m_{\text{sbi}} \left( k_h f B_{\text{sbi}}^\alpha \right) + m_{\text{teeth}} \left( k_e f B_{\text{teeth}}^\alpha \right) \end{aligned} \quad (58)$$

where  $k_e$  and  $k_h$  are eddy and hysteresis loss coefficients for a particular material, respectively, and  $\alpha$  is an exponential fit coefficient.

## IV. Mechanical Component Models

### A. Gas Generator Core

#### 1. Gas Generator Core Sizing

The gas generator core is sized using a power-law scaling of the core mass flow, which is based on the core shaft power,  $P_{\text{core}}$ , and an assumed specific power,  $P_{\text{sp}}$ :

$$\dot{m}_{\text{core}} = \frac{P_{\text{core}}}{P_{\text{sp}}} \quad (59)$$

$$m_{\text{core}} = K_{\text{core}} \dot{m}_{\text{core}}^{1.2}. \quad (60)$$

## 2. Gas Generator Core Performance

The core shaft power is related to the gas generator fuel mass flow,  $\dot{m}_{\text{fuel}}$ , through the heating value of the fuel,  $h_{\text{fuel}}$ , and an assumed cycle thermal efficiency  $\eta_{\text{th}}$ :

$$P_{\text{core}} = \eta_{\text{th}} \dot{m}_{\text{fuel}} h_{\text{fuel}}. \quad (61)$$

## B. Ducted Fan

### 1. Ducted Fan Sizing

The fan mass is sized using a power-law scaling of the fan diameter, which is estimated based on the performance requirements at the sizing condition (see below),

$$m_{\text{fan}} = K_{m,\text{fan}} d_{\text{fan}}^{2.4}. \quad (62)$$

### 2. Ducted Fan Performance

The fan shaft power,  $P_{\text{fan}}$ , is related to the net thrust power delivered,  $P_{\text{net}}$ , through the jet mass flow and velocity,  $\dot{m}_{\text{fan}}$  and  $V_{\text{jet}}$ , for an assumed fan efficiency,  $\eta_{\text{fan}}$ , and free stream flow velocity  $V_{\infty}$ :

$$P_{\text{net}} = \dot{m}_{\text{fan}} (V_{\text{jet}} - V_{\infty}) V_{\infty} \quad (63)$$

$$P_{\text{fan}} = \frac{\frac{1}{2} \dot{m}_{\text{fan}} (V_{\text{jet}}^2 - V_{\infty}^2)}{\eta_{\text{fan}}}. \quad (64)$$

The fan diameter is estimated based on the fan mass flow for an assumed flight condition, i.e., altitude and Mach number:

$$d_{\text{fan}} = K_{d,\text{fan}} \dot{m}_{\text{fan}}^{0.5}. \quad (65)$$

## C. Gearbox

### 1. Gearbox Sizing

The gearbox is sized based on an empirical correlation presented in Ref. [15]. Based on data from fifty rotorcraft, tiltrotor, and turboprop aircrafts, the authors found that the weight of the gearbox and its lubrication system,  $W_{\text{gb}}$  [lb], could be estimated using the fit [15]

$$W_{\text{gb}} = -37.4262 + 116.3297\beta \quad (66)$$

where  $\beta$  is the parametric value

$$\beta = \left( \frac{P}{\omega_{\text{out}}} \right)^{0.75} \left( \frac{\omega_{\text{in}}}{\omega_{\text{out}}} \right)^{0.15} \quad (67)$$

and  $P$  [hp] is the transmitted power,  $\omega_{\text{out}}$  [rpm] is the output angular speed, and  $\omega_{\text{in}}$  [rpm] is the input angular speed.

### 2. Gearbox Performance

The gearbox performance model relates input and output power with a specified efficiency:

$$\tau_{\text{out}} \omega_{\text{out}} = \eta_{\text{gb}} \tau_{\text{in}} \omega_{\text{in}} \quad (68)$$

where  $\tau_{\text{out}}$  and  $\tau_{\text{in}}$  are the output and input torques, respectively.

## V. Standalone Component Analysis

With the theory developed for the electrical and mechanical components in Sections III and IV, the SP framework can be used to optimize the design of individual components for different objectives, under various operating conditions, and using different material properties. This capability is demonstrated in this section using the electrical cable and motor models as examples.

### A. Optimum Cable Example

The higher fidelity cable model developed in Section III.C captures the trade-off in specific power and efficiency for cable design. It also captures the effect of operating the propulsion system at different voltage and current levels. The efficiency,  $\eta_c$ , of the cable can be expressed as

$$\eta_c = \frac{P_{\text{load}}}{P_{\text{source}}} = \frac{P_{\text{load}}}{P_{\text{load}} + I^2 R}. \quad (69)$$

Equation (69) shows that, for a fixed load power, the efficiency can be increased by either decreasing the resistance of the cable or decreasing the current.

First, the resistance of the cable is considered. From Eqn. (17), the cable resistance is a function of cable resistivity,  $\rho$ , length,  $\ell$ , and conductor cross-sectional area,  $A_c$ . Assuming the resistivity is fixed by the choice of conductor material and the length of the cable is fixed by the aircraft configuration, the cable resistance can only be decreased by increasing the conductor area,  $A_c$ . However, the mass of the cable is directly proportional to  $A_c$ . Therefore decreasing resistance will improve efficiency at the expense of increasing mass. Second, assuming the cable load voltage,  $V_{\text{load}}$ , is fixed, decreasing the cable current requires a larger source voltage,  $V_{\text{source}}$ . However, the necessarily larger source voltage increases the dielectric thickness of the cable from Eqn. 16, which also increases its mass.

Figure 8 shows both of these effects. This figure was generated by sweeping the cable efficiency at different voltage levels and using the SP optimizer to minimize mass. The sweep was conducted assuming a six meter cable, consisting of an aluminum alloy conductor and polyimide dielectric, that delivers 250 kW of power to a load. These parameters were chosen since they may be representative of a real aircraft cable. The material and design properties specified are summarized in Tables 2 and 3. Figure 8 illustrates that, at high voltage levels, there are diminishing marginal benefits for cable mass from further increasing voltage. However, at 100 V, the effect is significant. Finally, since the load power is fixed, Fig. 8 can be interpreted as illustrating that there is a trade-off between the specific power and efficiency of the cable.

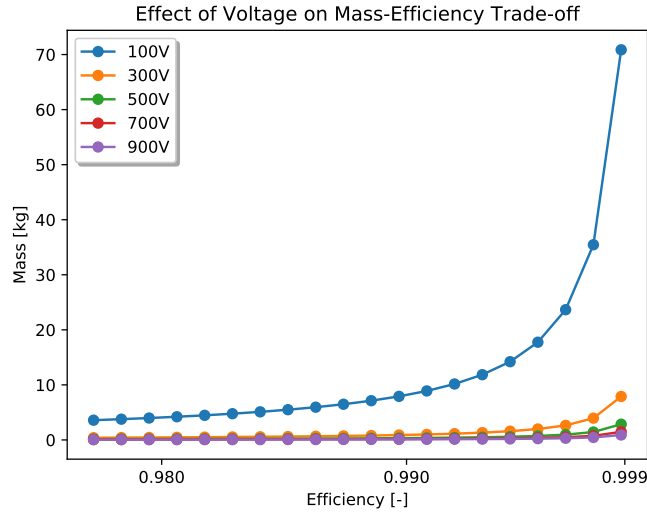


**Fig. 8** Increasing voltage improves the cable efficiency but gives diminishing marginal benefit.

### B. Optimum Motor Example

As mentioned in Section III.D, the motor model uses current-carrying conductors to link the magnetic flux from the rotor magnets. These motor windings have a similar mass and efficiency trade-off as the previous cable example, although the dielectric is not considered here. The cable model was used as a first example because the trade-off between its efficiency and mass can be immediately understood from its resistance and mass expressions. The motor, however, is more complicated. In addition to Ohmic heating losses, it has eddy current and hysteresis losses due to its rotating magnetic field, which are a function of its angular speed, number of pole pairs, and teeth and magnet mass. In total, the

**Table 2 Optimum cable study – fixed material properties.**

Parameter	Value
Conductor Density ( $d_c$ )	2830 kg/m <sup>3</sup>
Dielectric Density ( $d_{di}$ )	1700 kg/m <sup>3</sup>
Dielectric Strength ( $E_{max}$ )	10 <sup>7</sup> V/m
Resistivity ( $\rho$ )	$2.65 \cdot 10^{-8} \Omega \cdot m$

**Table 3 Optimum cable study – fixed design parameters.**

Parameter	Value
Packing Factor ( $k_{pf}$ )	0.91
Load Power ( $P_{load}$ )	250 kW
Cable Length ( $\ell$ )	6 m

motor model consists of 79 design variables where a change in one can affect several others. This section will show how the SP optimization approach can be used to gain insight into how these parameters trade-off.

This example considers a motor made of 29 Gage M-19 steel, neodymium magnets, and copper windings, similar to the design from Ref. [13]. The physical properties of these materials are summarized in Table 4. The eddy current and hysteresis loss parameters were obtained from Ref. [13]. In addition, several design parameters are fixed as shown in Table 5 that may be representative of a real motor design. This specific selection of parameters was fixed to highlight some trends of the motor mass and efficiency versus angular speed.

**Table 4 Optimum motor study – fixed material properties.**

Parameter	Value
Steel Density ( $d_{stator}, d_{rotor}$ )	8200 kg/m <sup>3</sup>
Magnet Density ( $d_{magnet}$ )	7501 kg/m <sup>3</sup>
Winding Density ( $d_{cond}$ )	8930 kg/m <sup>3</sup>
Winding Resistivity ( $\rho$ )	$1.67 \cdot 10^{-8} \Omega \cdot m$
Magnetization Constant ( $M$ )	$8.604 \cdot 10^{-5} A/m$
Saturation Flux Density ( $B_{sat}$ )	1.8 T
Hysteresis Loss Coefficient ( $k_h$ )	$10.664 \cdot 10^{-3} W/lb/Hz$
Eddy Current Loss Coefficient ( $k_e$ )	$32.183 \cdot 10^{-6} W/lb/Hz^2/T^2$

**Table 5 Optimum motor study – fixed design parameters.**

Parameter	Value
Mechanical Power ( $P_{mech}$ )	250 kW
Slot Current Density ( $J_s$ )	5 A/mm <sup>2</sup>
Pole Pairs ( $p$ )	8
Maximum Tip Speed ( $U_{max}$ )	200 m/s
Packing Factor $k_{pf}$	0.35

With these parameters fixed, the angular speed,  $\Omega$ , is swept from 250 rad/s to 20,000 rad/s and the SP optimizer solves the motor design with the objective of minimizing total motor mass. Figure 10 shows that the motor specific power improves with increasing angular speed. This trend is expected from Eqn. (48). Since  $P_{mech}$ ,  $p$ ,  $J_s$ , and  $k_{pf}$  are

fixed, the remaining degrees of freedom for meeting the mechanical power requirement are the tip radius,  $R_3$ , slot area,  $A_{\text{slot}}$ , air gap flux density,  $B_{\text{gap}}$ , axial length,  $\ell$ , and angular speed,  $\Omega$ . The former four parameters are related to geometry and increasing them increases mass, so instead it is desirable to increase  $\Omega$ , which only increases losses. This trend is captured in the efficiency plot. The nonlinear trade-off between efficiency and specific power is illustrated in Fig. 9.

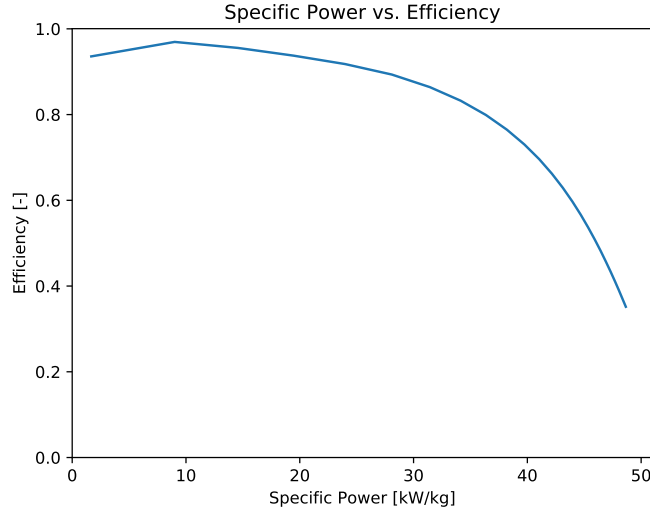


**Fig. 9 Trade-off between specific power and efficiency.**

At low rpm, the motor has a large torque requirement. Also a consequence of Eqn. (48), the machine is much heavier in this regime and is shown in Fig. 10. The reason is that the air gap flux density is limited to the magnet remanent flux density at best, which is approximately 1.1 T for the neodymium magnet being considered. This means the machine must have an increased tip radius, slot area, or axial length compared to the higher speed machines, resulting in the heavier components.

The initial increase in efficiency in Fig. 10 is due to a reduction in Ohmic heating losses. The peak efficiency represents the transition point where the eddy current and hysteresis losses begin dominating. Once the motor tip speed  $U_{\text{max}}$  is reached, the tip radius  $R_3$  is now specified by  $R_3 = U_{\text{max}}/\Omega$ , so the machine geometry can only be changed on the stator side or by increasing its axial length. A combination of the two occurs as indicated from the near-constant teeth mass in Fig. 10.

Lastly, Fig. 11 shows the top sensitivities for the highest specific power motor in Fig. 10. These sensitivities provide some practical insight into whether the objective can be improved. In this figure, red bars show parameters that would decrease mass if increased, whereas blue bars show parameters that would increase mass if increased. The numbers at the end of the bar represent the percent change that would occur if this parameter was changed 1%. Since the load power is fixed, the top sensitivities considered here are the steel saturation, winding current density, and tip speed limit. The steel saturation could be improved using alternative materials such as Hiperco-50. The peak winding current density was fixed using a number typical of industry machines. In practice, this is limited by cooling. Finally, at high tip speeds, the motor begins to have issues with structural integrity and rotordynamics. In lieu of a model for these considerations, a fixed tip speed limit based on the survey from Ref. [16] is used.

## VI. Turboelectric System Analysis

Sections V.A and V.B demonstrated that there is a trade-off between specific power and efficiency for electrical cables and machines. These two performance metrics are emphasized in component design for electric aircraft propulsion since efficiency affects overall fuel or energy consumption and specific power affects the mass of the propulsion system. The relative importance of each depends on the aircraft and mission, so this section demonstrates how the SP approach coupled with the developed electrical and mechanical models can be used to explore the propulsion system trade space.

In this section, a turbofan, an AC turboelectric, and a geared AC turboelectric system are compared on the metrics of fuel mass flow (i.e., fuel consumption) and mass. The AC turboelectric assumes a “direct-drive” configuration in which



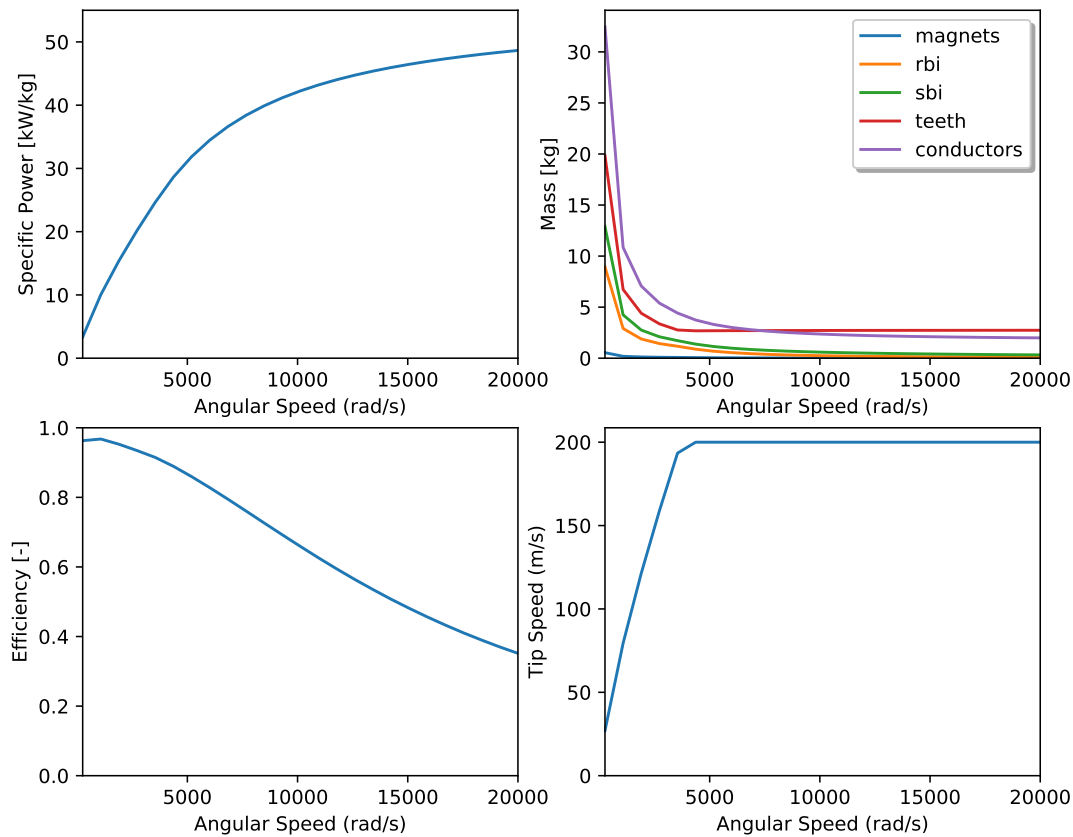


**Fig. 10** Subplots showing optimized motor specific power (top left), motor component masses (top right), efficiency (lower left), and tip speed (lower right) versus angular speed.

the generator is directly connected to the motor via cables, and then the motor directly drives a shaft-mounted fan. In this configuration, the turboshaft and motor shaft speeds are related by the ratio of pole pairs between the motor and generator. In the geared AC turbosystem, a gearbox is placed between the generator and motor. This allows the motor to optimize its angular speed and number of pole pairs. These three architectures are illustrated in Fig. 12.

To demonstrate the utility of signomial programming for studying these architectures, specific materials and design parameters were chosen that enable the generation of Pareto frontiers of fuel consumption versus mass for each architecture. The electrical machines are assumed to use 29 Gage M-19 steel with neodymium magnets which have the material properties listed in Table 4. The cables are also assumed to consist of an aluminum alloy conductor and polyimide tape dielectric, the properties of which are listed in Table 2. The turboshaft model does not include the effect of angular speed, so the generator shaft speed is fixed to 9,000 rpm. Some additional parameters, summarized in Table 6, were chosen such that the models can be swept across the same range of mass values.

Figure 13 shows the trade-off between fuel consumption and mass for the three architectures. The turbofan architecture is lighter and more efficient than the two turbosystem architectures, which suggests that there is no system-level benefit to decoupling the turboshaft and fan speeds through the use of generators and motors under this specific set of assumptions, e.g., without any change to the number of propulsors, integration into the airframe, or other potential system-level benefits enabled by electrification. If turbosystem was to be used, the AC direct drive turbosystem architecture is generally better for minimizing propulsion system mass because the geared turbosystem includes the additional weight of the gear. However, the geared AC turbosystem is generally better for minimizing fuel flow rate

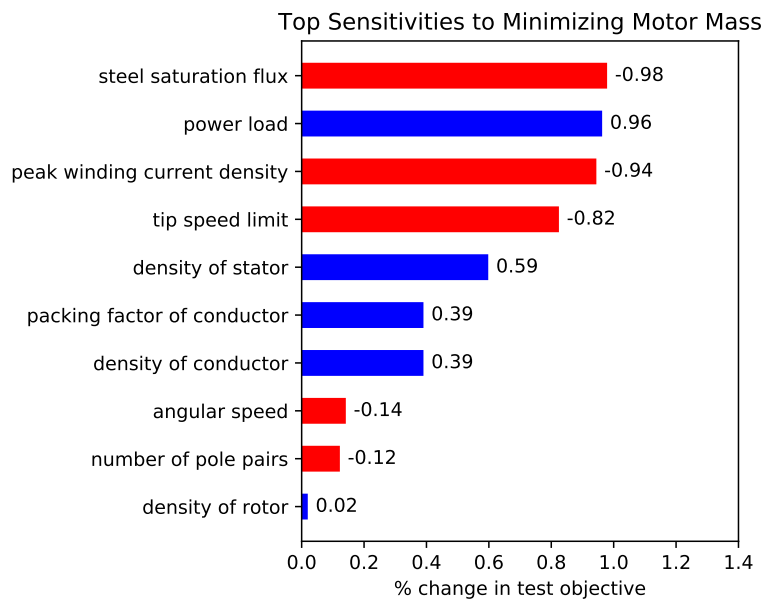


**Fig. 11 Top sensitivities for minimizing motor mass at 20,000 rad/s.**

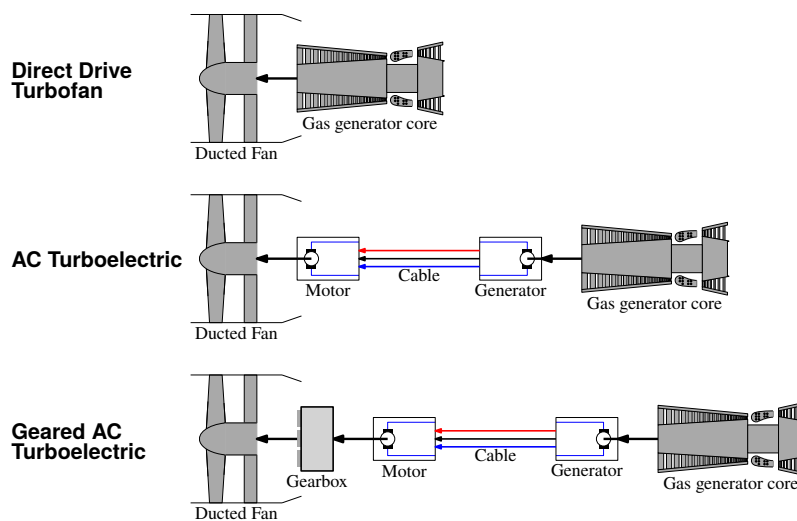


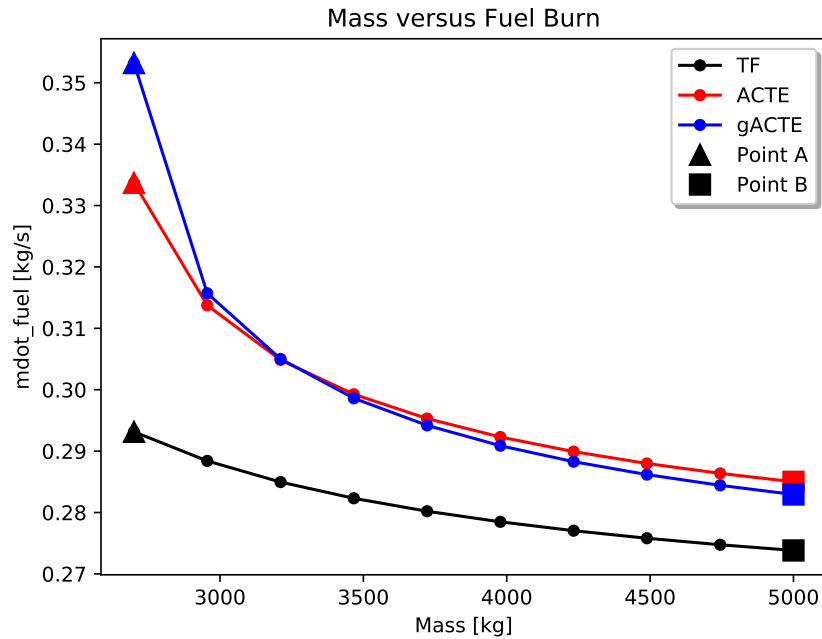
**Fig. 12 Diagrams of the turbofan, AC turboelectric, and geared AC turboelectric architectures.**

because decoupling the motor and fan shaft speeds allows for a larger fan with higher propulsive efficiency.

This example also demonstrates that the component designs can completely change depending on where the system lies along the Pareto frontiers. An example is the motor model. Data was collected from both the minimum mass and minimum fuel consumption points in the AC turboelectric curve in Fig. 13. Shown in Fig. 14, the motor mass is heavier at the minimum mass point than it is at the minimum fuel consumption point. This is counterintuitive, but it is a consequence of the electric fan mass and efficiency trade-off. At the minimum mass point, the propulsive efficiency of the fan is just 80%, and so the motor has to be sized for a much larger power requirement. At the minimum fuel consumption point, the propulsive efficiency is approximately 93% efficient but the fan weighs four times as much. The efficiency and component mass breakdowns that illustrate these trades are shown in Figs. 15 and 16, respectively.

**Table 6 Optimum propulsion system study – fixed design parameters.**

Component	Parameter	Value
Turboshaft	Core Mass Constant ( $K_{\text{core}}$ )	45.605 kg/(kg/s) <sup>1.2</sup>
	Core Specific Power ( $P_{\text{sp}}$ )	400 kJ/kg
	Kerosene specific energy ( $h_{\text{fuel}}$ )	43 MJ/kg
	Core thermal efficiency ( $\eta_{\text{th}}$ )	0.5
Generator	Mechanical Power ( $P_{\text{mech}}$ )	250 kW
	Slot Current Density ( $J_s$ )	5 A/mm <sup>2</sup>
	Pole Pairs ( $p$ )	10
	Tip Speed ( $U$ )	200 m/s
	Slot Current Density $J_s$	15 A/mm <sup>2</sup>
	Angular Speed ( $\Omega$ )	9,000 rpm
	Voltage $V_{\text{rms}}$	1000 V
Cable	Length ( $\ell$ )	6 m
Motor	Slot Current Density ( $J_s$ )	15 A/mm <sup>2</sup>
	Max Tip Speed ( $U_{\text{max}}$ )	200 m/s
Gearbox	Gearbox Efficiency $\eta_{\text{gb}}$	1.0
Fan	Net Propulsive Power $P_{\text{net}}$	5 MW
	Max Fan Tip Mach No. $M_{\text{tip,max}}$	1
	Fan Efficiency $\eta_{\text{tip,max}}$	0.9
	Fan Diameter Constant ( $K_{\text{d,fan}}$ )	154 kg/m <sup>2.4</sup>
	Fan mass Constant ( $K_{\text{m,fan}}$ )	0.137 m/(kg/s) <sup>0.5</sup>

**Fig. 13 Trade-off between fuel flow and total propulsion mass for the turbofan (TF), AC turboelectric (ACTE), and geared AC turboelectric (gACTE) architectures.**

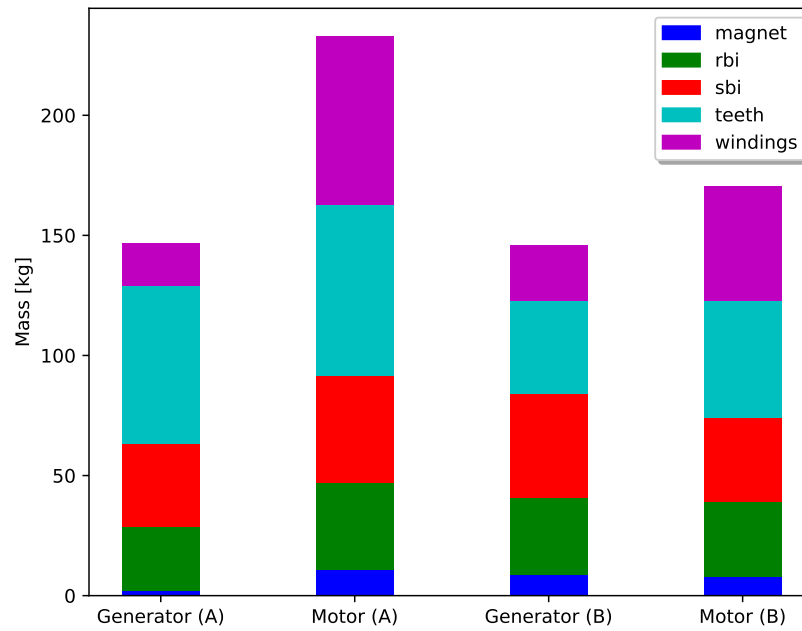


**Fig. 14** Breakdown of the generator and motor constituent masses at the minimum mass point, A, and minimum fuel point, B, for the ACTE architecture.

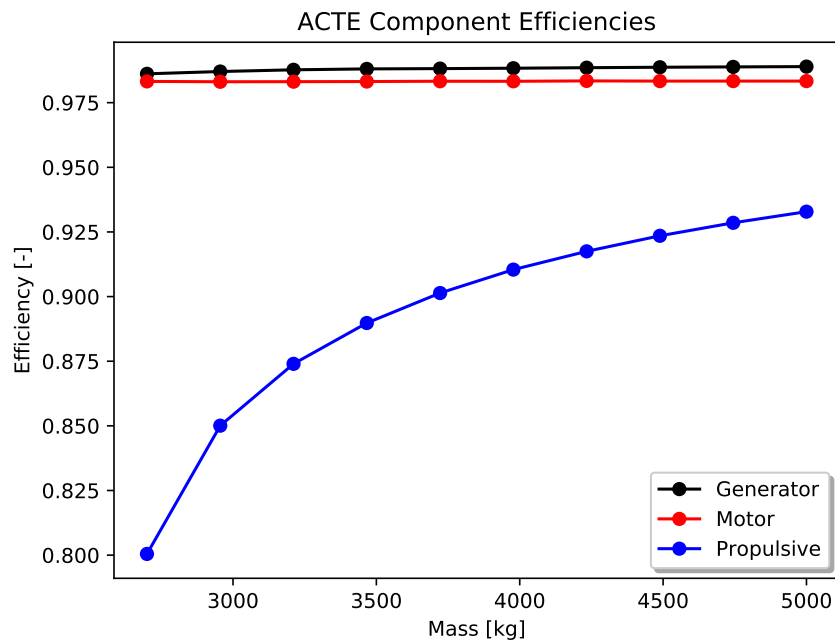


**Fig. 15** An efficiency versus mass plot for the ACTE architecture shows that the fan propulsive efficiency increases for lower fuel flow, whereas the electrical component efficiencies remain relatively constant.

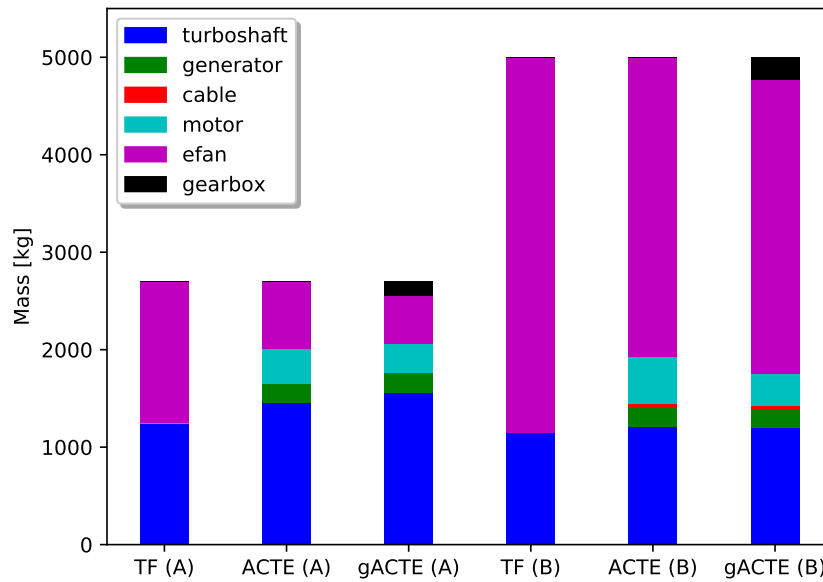


**Fig. 16 Breakdown of the propulsion component masses at the minimum mass point, A, and the minimum fuel consumption point, B.**

## VII. Conclusions and Future Work

This paper has demonstrated that detailed propulsion system component models can be used in conjunction with the multi-disciplinary optimization technique of signomial programming to assess electric propulsion systems. First, the development of SP-compatible sizing and performance models was shown for the battery, cable, generator/motor, turboshaft, fan, and gearbox models. These models vary in fidelity, with the power electronics model being a specified efficiency and specific power, whereas the motor model considers the geometry, torque-speed requirements, and materials used.

For future work, the fidelity of all of these models could be improved. Despite their high efficiencies, the electrical components will still dissipate a large amount of heat at high power levels. However, a thermal management system was not considered in this paper; instead, simplifying assumptions were used. For example, for the electrical machine models, the current density was fixed to a number typical of industry machines, and their magnets and windings were assumed to be at 120°C. In addition, the thermal management for the power electronics is expected to represent a significant fraction of its weight. Thus, thermal modeling remains as open work. Some additional component modeling improvements are adding speed dependency to the turboshaft model and considering other types of electrical machines, such as induction or variable reluctance.

Next, the electrical and mechanical propulsion component models were used in turbofan, AC turboelectric, and geared AC turboelectric propulsion architectures. Pareto frontiers of fuel consumption and propulsion system mass were generated by optimizing these architectures using the SP solver. These Pareto frontiers are useful because, without an airframe or mission, it is unclear whether fuel flow rate or propulsion system mass is more important. In addition, two of the Pareto frontier points were considered in more detail to show that the component designs can deviate significantly from their standalone optima. For example, for the AC turboelectric system, the motor for the lightest system is over 60 kg heavier than the motor for the most efficient, but heaviest, system.

Examples with the battery model were not shown because the battery requires total mission energy, but only a power requirement was considered in this paper. References [7] and [8] show the use of the battery model but with the rest of the propulsion system described by specified efficiency and specific power. However, future work would include integrating these more detailed propulsion system models with airframe and mission models, of which detailed ones

were demonstrated to be SP-compatible in Ref. [6]. This would enable all of the other propulsion architectures from Fig. 1 and Ref. [3] to be considered.

### Acknowledgments

This work was supported by the Leading Edge Aeronautics Research for NASA (LEARN) project, awarded under solicitation NNH15ZEA001N-LEARN3, and the NASA Aeronautics Graduate Scholarship Grant No. NNX17AB22H. The authors would like to thank W. H. Hoburg and E. E. Burnell of MIT for their assistance with the GPkit framework, E. M. Greitzer, Z. S. Spakovszky, and J. S. Sabnis of MIT and S. Byahut, M. Kruger, and A. Uranga of USC for their guidance over the course of the LEARN project, and R. F. Beach and R. H. Jansen for their helpful feedback during LEARN reviews.

### References

- [1] Felder, J.L., Kim, H.D., and Brown, G.V., "Turboelectric Distributed Propulsion Engine Cycle Analysis for Hybrid-Wing-Body Aircraft," 47th AIAA Aerospace Sciences Meeting include The New Horizons Forum and Aerospace Exposition, Aerospace Sciences Meetings, 2009.  
doi:10.2514/6.2009-1132
- [2] Bradley, M. K., and Droney, C. K., "Subsonic Ultra Green Aircraft Research: Phase I Final Report," NASA CR-2011-216847, April 2011.
- [3] National Academies of Sciences, Engineering, and Medicine, *Commercial Aircraft Propulsion and Energy Systems Research: Reducing Global Carbon Emissions*, National Academy Press, 2016.
- [4] Brown, G.V., "Weights and Efficiencies of Electric Components of a Turboelectric Aircraft Propulsion System," 49th AIAA Aerospace Sciences Meeting including the New Horizons Forum and Aerospace Exposition, Aerospace Sciences Meetings, AIAA Paper 2011-225, 2011.
- [5] Jansen, R.H., Brown, G.V., Felder, J.L., and Duffy, K.P., "Turboelectric Aircraft Drive Key Performance Parameters and Functional Requirements," 51st AIAA/SAE/ASEE Joint Propulsion Conference, AIAA Propulsion and Energy Forum, AIAA Paper 2015-3890, 2015.
- [6] Hall, D.K., Dowdle, A.P., Gonzalez, J.J., Trollinger, L., and Thalheimer, W., "Assessment of a Boundary Layer Ingesting Turboelectric Aircraft Configuration using Signomial Programming," to appear, AIAA AVIATION Forum, 2018.
- [7] Kruger, M., Byahut, S., Uranga, A., Dowdle, A., Gonzalez, Hall, D.K., "Electrified Aircraft Trade-Space Exploration," to appear, AIAA AVIATION Forum, 2018.
- [8] Hall, D.K., Greitzer, E.M., Dowdle, A.P., Gonzalez, J.J., Hoburg, W.W., Ilic, M., Lang, J.H., Sabnis, J.S., Spakovszky, Z.S., Yutko, B., Courtin, C., Thalheimer, W., Trollinger, L., Tylko, J., Varney, N., Uranga, A., Byahut, S., and Kruger, M., "Feasibility of Electrified Propulsion for Ultra-Efficient Commercial Aircraft, Final Report," NASA CR to appear, 2018.
- [9] Zhang, X., and Haran, K., "High-Specific-Power Electric Machines for Electrified Transportation Applications – Technology Options," IEEE Energy Conversion Congress and Exposition (ECCE), 2016.
- [10] Burnell, E., and Hoburg, W., "GPkit Software for Geometric Programming," <https://github.com/convexengineering/gpkit>, Version 0.7.0, 2018.
- [11] Kirschen, P. G., Burnell, E. E., and Hoburg, W. H., "Signomial Programming Models for Aircraft Design," 54<sup>th</sup> AIAA Aerospace Sciences Meeting, AIAA SciTech Forum, AIAA Paper No. 2016-2003.  
doi:10.2514/6.2016-2003
- [12] Farve, N., "Design of a Low-Mass High-Torque Brushless Motor for Application in Quadruped Robotics," S.M. Thesis, Massachusetts Institute of Technology, Cambridge, MA, 2012.
- [13] Ofori-Tenkorang, J., "Permanent-Magnet Synchronous Motors and Associated Power Electronics for Direct-Drive Vehicle Propulsion," Ph.D. Dissertation, Massachusetts Institute of Technology, Cambridge, MA, 1996.
- [14] Riddle, R.R., and Dix, D.M., *Technology Assessment of Advanced Propulsion Systems for Some Classes of Combat Vehicles, Volume III*, Institute for Defense Analyses, 1979.

- [15] Tong, M.T., Jones, S.M., Haller, W.J., and Handschuh, R.F., "Engine Conceptual Design Studies for a Hybrid Wing Body Aircraft," NASA TM-2009-21580, 2009.
- [16] Gerada, D. and Mebarki, A. and Brown, N.L. and Gerada, C. and Cavagnino, A. and Boglietti, A. "High-Speed Electrical Machines: Technologies, Trends, and Developments," *IEEE Transactions on Industrial Electronics*, Vol. 61, No. 6, June 2014.